Finding Magnetopause Standoff Distance using a Soft X-ray Imager – Part 1: Magnetospheric masking

Andrey Samsonov[1], Jennifer Alyson Carter[2], Andrew Read[2], Steven Sembay[2], Graziella Branduardi-Raymont[1], David Sibeck[3], Philippe Escoubet[4]

[1]Mullard Space Science Laboratory, University College London, UK
[2]Leicester University, UK
[3]Goddard Space Flight Center NASA, USA
[4]ESA/ESTEC, Noordwijk, The Netherlands

Key Points:

- The SMILE mission will carry Soft X-ray Imager onboard
- Magnetospheric masking methods separate the magnetosphere from the magnetosheath and cusps

Corresponding author: Andrey Samsonov, a.samsonov@ucl.ac.uk

Abstract

The magnetopause standoff distance characterizes global magnetospheric compression and deformation in response to changes in the solar wind dynamic pressure and interplanetary magnetic field orientation. We cannot derive this parameter from in-situ spacecraft measurements. However, time-series of the magnetopause standoff distance can be obtained in the near future using observations by soft X-ray imagers. In two companion papers, we describe methods of finding the standoff distance from X-ray images. In Part 1, we present the results of MHD simulations which we use for the calculation of the X-ray emissivity in the magnetosheath and cusps. Some MHD models predict relatively high density in the magnetosphere, larger than observed in the data. Correcting this, we develop magnetospheric masking methods to separate the magnetosphere from the magnetosheath and cusps. We simulate the X-ray emissivity in the magnetosheath for different solar wind conditions and dipole tilts.

Plain Language Summary

The highly dynamic solar wind continuously bombards the Earth's magnetosphere, which changes shape in response. The magnetopause is the outer boundary of the magnetosphere, which is known to move. We are limited in our knowledge of the overall shape of the magnetopause, as current in situ measurements can only tell us about any change in the magnetopause at one specific location. Spacecraft carrying soft X-ray imagers, however, will soon revolutionise our understanding by monitoring large areas of the magnetopause as the solar wind varies. In this first of a series of two papers, we simulate X-ray emissions in the vicinity of the Earth using two magnetohydrodynamic models, and for two case studies with vastly different incoming solar wind conditions. In a subsequent paper, we examine methods how to extract the magnetopause shape from the simulated X-ray images.

1 Introduction

The Earth's magnetopause is the boundary between the geomagnetic and interplanetary magnetic fields. The magnetopause standoff distance, i.e. the distance from the Earth to the subsolar magnetopause, implicitly characterizes the magnetospheric activity. A more compressed magnetosphere results in stronger magnetospheric-ionospheric currents and correspondingly higher magnetospheric activity. When the magnetopause crosses geosynchronous orbit, spacecraft that rely upon observations of the Earth's magnetic field to determine their orientation may lose this information. Therefore we would like better predict the magnetopause position for variable solar wind conditions.

The magnetopause standoff distance is usually determined by the pressure balance condition. Up to now, we have been able to find the magnetopause position for a given solar wind condition by three methods. First, we can use direct in-situ measurements. This method gives us the exact magnetopause position, but only in one or several local points and at the time when the spacecraft crosses the magnetopause. Second, we can apply empirical magnetopause models (e.g., Dmitriev et al., 2016; Lin et al., 2010; Petrinec & Russell, 1996; Shue et al., 1998; Sibeck et al., 1991; Wang et al., 2013). Empirical models are usually based on large datasets of magnetopause crossings and use predefined functional forms to describe an expected magnetopause shape. However, any fixed function may not perfectly reproduce the real magnetopause shape. Besides, we do not know exactly the list of input parameters which may influence the magnetopause position since this list could possibly include characteristics of the magnetospheric currents (e.g. the ring current, magnetospheric-ionospheric region 1 and 2 currents, the cross-tail current) in addition to the upstream solar wind conditions. Moreover, some solar wind parameters (e.g., the interplanetary magnetic field (IMF) Bx component) may change the total pressure upstream of the magnetopause (e.g., Archer et al., 2015; Samsonov et al.,

2017), but they are not included in the empirical models. Third, the magnetopause position can be found from results of global magnetohydrodynamic (MHD) as well as hybrid or kinetic simulations. However, numerical models have some limitations, for example MHD models do not simulate self-consistently some magnetospheric currents (e.g. the ring current) and often rely upon a possibly unphysical numerical resistivity. Therefore each of the three methods is not perfect for finding the magnetopause standoff distance and shape. This is especially true for extreme solar wind conditions because we have a very limited number of observations at these times and models may be less accurate.

Gordeev et al. (2015); Samsonov et al. (2016) showed that the simulated magnetopause positions obtained for typical solar wind conditions differ between several global MHD models. For example, the magnetopause standoff distance predicted by the Lyon-Fedder-Mobarry (LFM) and Open Geospace General Circulation Model (Open GGCM) models is 0.5-1.5 R_E less (i.e., closer to the Earth) than that in the Space Weather Modeling Framework (SWMF) model for the same solar wind conditions. There are several reasons for the difference. Firstly, the magnetopause position is determined by the pressure balance condition. The total pressure on the inner side of magnetopause is mostly the magnetic pressure which consists of the dipole field and the superposition of magnetic fields of the magnetospheric currents, like the Chapman-Ferraro current, the ring current, the magnetospheric-ionospheric region 1 current, and to a lesser extent the cross-tail current (Tsyganenko & Sibeck, 1994). Although the magnetospheric thermal pressure is generally insignificant compared to the magnetic pressure, it can also make some input in the pressure balance. Different MHD models use different boundary conditions at the inner numerical boundary (usually at radial distance of about 2–3 R_E from the Earth) which result in different magnetospheric densities and thermal pressure, in particular in the dayside magnetosphere. Beside that, some models try to include the ring current, and some do not. As a result, the total magnetospheric pressure varies between the models.

The total pressure on the outer side of magnetopause is often supposed to be equal to the solar wind dynamic pressure but this assumption is not very accurate. Samsonov et al. (2012) using MHD simulations calculated the variations of the total pressure (i.e., the sum of the dynamic, thermal and magnetic pressures) through the subsolar magnetosheath. Since the magnetosheath in the subsolar region is a layer with a width great than 1 R_E (typically about 3 R_E), the total pressure changes through the magnetosheath and these changes depend on the IMF orientation. Therefore differences in the inner boundary conditions and in the numerical methods between the MHD models may result in a different total pressure at the magnetopause which in turn influences the magnetopause position.

Moreover, the magnitudes of the magnetopause electric currents may depend on the numerical resolution of MHD models as well as on the type of diffusion term applied in the models (e.g., the total variation diminishing (TVD) slope limiter) and on the order of accuracy of the numerical scheme. The stronger the magnetopause currents near the subsolar point, the smaller the magnetopause standoff distance (Tsyganenko & Sibeck, 1994). This might be another reason which explains the differences between the models.

Empirical magnetopause models do not agree well with each other in predicting the magnetopause standoff distance either (Samsonov et al., 2016). Axisymmetric magnetopause models cannot reproduce the cusp indentations or the changes related to the dipole tilt effect, and most of them predict the subsolar magnetopause to be closer to the Earth than non-axisymmetric models for typical solar wind conditions and zero tilt angle. Case and Wild (2013) compared predictions of the axisymmetric and non-axisymmetric empirical models with Cluster magnetopause crossings (mostly in the high-latitude region) and found that, on average, the Petrinec and Russell (1996) and Shue et al. (1998)

models overestimate the radial distance to the magnetopause by 1 R_E, while the Dmitriev and Suvorova (2000) and Lin et al. (2010) models underestimate it by 0.5 R_E and 0.25 R_E, respectively. Moreover, two non-axisymmetric models (Lin et al., 2010; Wang et al., 2013) predicted different magnetopause positions on the Sun–Earth line and in the terminator plane (Samsonov et al., 2016). In general, the scattering of predictions of the magnetopause standoff distance for typical solar wind conditions between empirical and MHD models may be about 2 R_E (Samsonov et al., 2016).

Recent studies show that the Earth's magnetosheath and cusps are sources of soft X-rays with energies from 0.05 to 2.0 keV (e.g., Carter et al., 2010; Cravens et al., 2001; Kuntz et al., 2015; Robertson et al., 2006). The soft X-rays result from the interaction between heavy solar wind ions (e.g. O^7+) and exospheric neutrals (hydrogen). Using a soft X-ray detector, we can produce two-dimensional (2-D) images of the X-rays around the magnetosphere. By processing these images we can find the magnetopause position (Branduardi-Raymont et al., 2012; Collier et al., 2012; Collier & Connor, 2018; Sibeck et al., 2018; Sun et al., 2019; Walsh et al., 2016). The Soft X-ray Imager (SXI) will travel onboard a joint space mission of the European Space Agency and the Chinese Academy of Sciences. The name of the mission is Solar wind Magnetosphere Ionosphere Link Explorer (SMILE) (Branduardi-Raymont et al., 2018). Besides the SXI, SMILE carries the Ultra Violet Imager (UVI), a magnetometer, and a plasma instrument for in-situ measurements of the solar wind and magnetosheath parameters. SMILE is due to launch in early 2025 into a highly elliptical orbit with apogee of about 19 R_E, inclination angle of 70 or 98 degrees depending on launcher, and orbital period of about 50 hours. Using the SXI, we can obtain continuous time-series of the magnetopause standoff distance for variable solar wind conditions.

In the two companion papers, we simulate the expected output of the SXI and present the methods of finding the magnetopause standoff distance from X-ray images. We use the results of global MHD simulations to calculate the X-ray emissivity in geospace. In Part 1, we present the results of simulations for two events, using two numerical models. We discuss finding the magnetopause position in the simulations and explain possible reasons for differences between the models. Some MHD models predict the density in the magnetosphere to be higher than has been observed, and we, therefore, introduce several methods of magnetospheric masking by highlighting grid points located in the magnetosphere. In Part 2, we will discuss the simulation and processing of X-ray images and show how we can find the magnetopause position from them.

2 Models and Boundary Conditions

We use the SWMF global MHD model (Tóth et al., 2005, 2012) version 20180525 and the Lyon-Fedder-Mobarry magnetosphere–ionosphere model (LFM–MIX) (Lyon et al., 2004; Merkin & Lyon, 2010) version LTR-2_1_5 available through the runs on request from the Community Coordinated Modeling Center at Goddard Space Flight Center. The SWMF model uses an adaptive structured Cartesian grid with highest resolution in the inner magnetosphere (Powell et al., 1999). In this study, we use runs with the best spatial resolution of 0.125 R_E in the whole dayside magnetosphere and magnetosheath. The resolution in the nightside magnetosphere ($x < -4$ R_E), upstream of the bow shock, and on the flanks near the terminator plane is 0.25 R_E or worse. The LFM model uses a distorted spherical grid with spatial resolution along the x axis in the subsolar magnetosphere close to that in the SWMF model. In both models, the low-altitude numerical boundary is located at a radial distance of $R \simeq 2{-}3$ R_E. The density at this boundary in the SWMF model is usually fixed and equal to 28 cm^{-3}. In the LFM model, the radial gradient of the density at the inner boundary is fixed to be equal to zero (Xi et al., 2015). The solar wind enters into the numerical region through another boundary located relatively far upstream of the bow shock, e.g. at $x = 30$ R_E (LFM) or 33 R_E (SWMF).

We simulate two cases in this study. The first case is an artificial case with constant solar wind conditions: the ion density $N_{SW} = 12.25$ cm^{-3}, the velocity along Sun-Earth line 400 km/s, $B_X = B_Y = 0$, $B_Z = 5$ nT. These velocity and magnetic field modulus values are close to the average, while the density is moderately higher than average. As a result, the magnetosphere is slightly compressed in this case. The ionospheric Pedersen conductance is constant and equal to 5 mho.

In the second case, we use solar wind conditions from the Wind spacecraft on June 16-17, 2012. This event consists of a large interplanetary coronal mass ejection (ICME) simulated in the heliosphere by Shen et al. (2014) and characterized by a large solar wind density with a brief interval of extremely high values up to 100 cm^{-3} during a long northward IMF interval. The auroral emission, ionospheric currents and convection in this event have been studied by Carter et al. (2020). In this case, we employ a statistical auroral ionosphere conductance model driven by the solar irradiation index (F10.7) and by the FAC patterns (Ridley et al., 2004).

The solar wind conditions in the second case are shown in Figure 1. The whole time interval from 17:00 UT on 16 June to 12:00 UT on 17 June 2012 has been simulated, but only several selected times, i.e., 20:00, 22:25, and 23:10 on 16 June and 00:00 UT on 17 June, are analyzed in detail below. The solar wind parameters in Figure 1 are time-shifted from the Wind position near Lagrangian point L1 to the upstream numerical boundary ($x = 33\ R_E$ for the SWMF model). However, we should also take into account the propagation time from this boundary to the subsolar magnetopause if studying the variations of the standoff distance. If we estimated the time lag using the solar wind velocity observed by Wind, we would underestimate this lag because the velocity in the magnetosheath is on average a few times less than in the supersonic solar wind upstream of the bow shock. Samsonov et al. (2017, 2018) showed that the average propagation time of directional discontinuities across the magnetosheath for typical solar wind conditions is about 14 min, and this time lag depends on how strongly the velocity drops down in the magnetic barrier ahead of the magnetopause. In the case presented here, the solar wind speed changes and remains higher than a typical one after 20:22 UT when the interplanetary shock arrives at the upstream boundary, therefore we estimate the propagation time between the solar wind boundary and magnetopause to be equal to 10 min. We use this time lag for the SWMF model, while by checking temporal variations of MHD parameters upstream of the bow shock we conclude that a more appropriate time lag for the LFM model is 5 min. In Table 1, we provide the solar wind conditions at 19:50, 22:15, 23:00, and 23:50 UT (i.e. 10 min before the times of magnetospheric response mentioned above) as well as the dipole tilt and magnetopause standoff distance in the empirical and MHD models. We compare the magnetopause positions obtained in MHD simulations with the two empirical magnetopause models (Shue et al., 1998; Lin et al., 2010).

The soft X-ray emissivity P_x is found to be proportional to the ion density N_{SW} in the solar wind and magnetosheath, the exospheric neutral density N_H, and the relative velocity V_{rel}.

$$P_x = \alpha N_{SW} N_H V_{rel}, \quad \text{here} \quad \alpha = 10^{-15} eVcm^2 \tag{1}$$

The interaction efficiency factor α depends on the charge transfer cross section, the fraction of high charge state ion species in the solar wind, transition energy and other factors. This estimate of α agrees with previous studies (e.g., Cravens, 2000; Pepino et al., 2004; Sun et al., 2019; Wegmann et al., 1998).

The exospheric neutral density N_H falls off with R^{-3} where R is a geocentric distance (Cravens et al., 2001). According to this model, the neutral density at the radial distance of 10 R_E, i.e. near the subsolar magnetopause for typical solar wind conditions, is equal to 25 cm^{-3}.

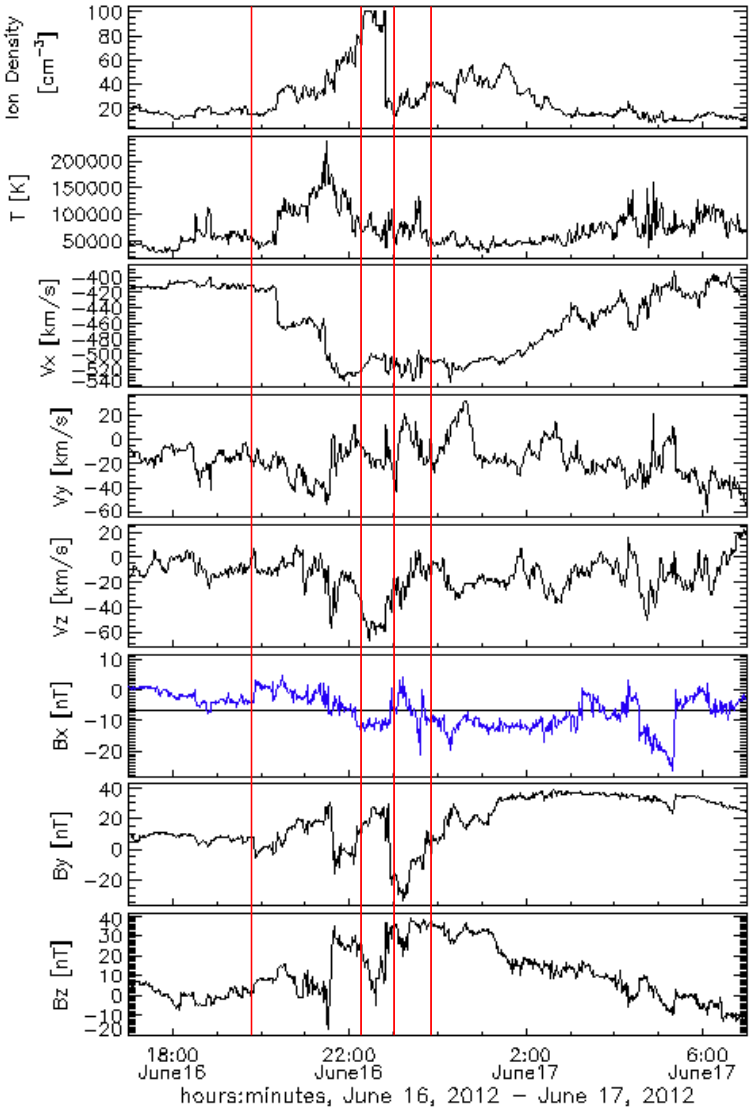

Figure 1. Solar wind parameters observed by Wind on June 16-17, 2012. Vertical red lines mark the four selected times (19:50, 22:15, 23:00, and 23:50 UT) used for the following analysis taking into account the 10 min time lag between the solar wind boundary and magnetopause (see details in text).

Table 1. Solar wind parameters (top rows 1-3) at selected times on June 16, 2012. Bottom part shows: the Earth dipole tilt (row 1), the magnetopause standoff distance predicted by the empirical Shue et al. (1998) (row 2) and Lin et al. (2010) (row 3) models, the standoff distance in the SWMF (row 4) and LFM (row 5) simulations. We apply the time lags of 5 and 10 min to the LFM and SWMF simulations respectively to take into account the propagation time from the inflow boundary to the subsolar magnetopause.

UT	19:50	22:15	23:00	23:50
Density, cm^{-3}	14.9	74.6	14.7	39.1
Velocity, km/s	411	523	519	513
B_Z, nT	1.1	23.3	34.4	36.5
Tilt, degr.	29.8	24.1	22.2	20.1
R_{SHUE}, R_E	9.2	6.7	8.6	7.5
R_{LIN}, R_E	9.0	6.1	8.2	6.9
R_{SWMF}, R_E	8.4	5.8	7.4	6.6
R_{LFM}, R_E	9.0	6.1	7.4	7.0

3 MHD simulations

3.1 Case 1

We exploit the SWMF and LFM models to reproduce the magnetospheric configuration and obtain input conditions for the following simulations of SXI images. Using this stationary case with a purely northward IMF, we display several differences between the models which may result in different magnetopause standoff distances. One such difference is related to the boundary conditions at the inner numerical boundary. Figure 2 displays the density obtained in the equatorial plane for the SWMF (left) and LFM (right) models. The magnetospheric density in the SWMF model is nearly one order of magnitude higher than that in the LFM model. Therefore, while the magnetopause position can be clearly identified using the density distribution in the LFM model, the density changes through the subsolar magnetopause might vary too smoothly for unambiguous determination of the magnetopause standoff distance in the SWMF results.

The inner boundary conditions seem to play a minor role in differences of the magnetopause standoff distance. Since the standoff distance is controlled by the pressure balance condition, we show profiles of the pressure components and total pressures along the Sun-Earth line in Figure 3. In the solar wind upstream of the bow shock, the dynamic pressure is about two orders of magnitude higher than either thermal or magnetic pressures. At the bow shock, the dynamic pressure decreases while both the thermal and magnetic pressures increase. In general, the total pressure (i.e. the sum of dynamic, thermal, and magnetic pressures) is supposed to be conserved through the bow shock according to the Rankine-Hugoniot conditions. However, the total pressure can change through the magnetosheath since the magnetosheath is a thick layer several R_E wide (Samsonov et al., 2012). Further, the total pressure does not change through the magnetopause because the magnetopause is a tangential discontinuity in the northward IMF case.

Since the bow shock in MHD simulations is always a layer (with a width of several grid spacings) rather than a discontinuity due to the numerical dissipation, we do not expect that the total pressure stays exactly the same on both sides of the bow shock. Indeed, Figure 3 shows that the total pressure changes in a different way through the bow shock in the SWMF and LFM models. The SWMF model predicts a small ($\sim 3\%$) decrease in the total pressure which may be a precursor of the following decreasing trend

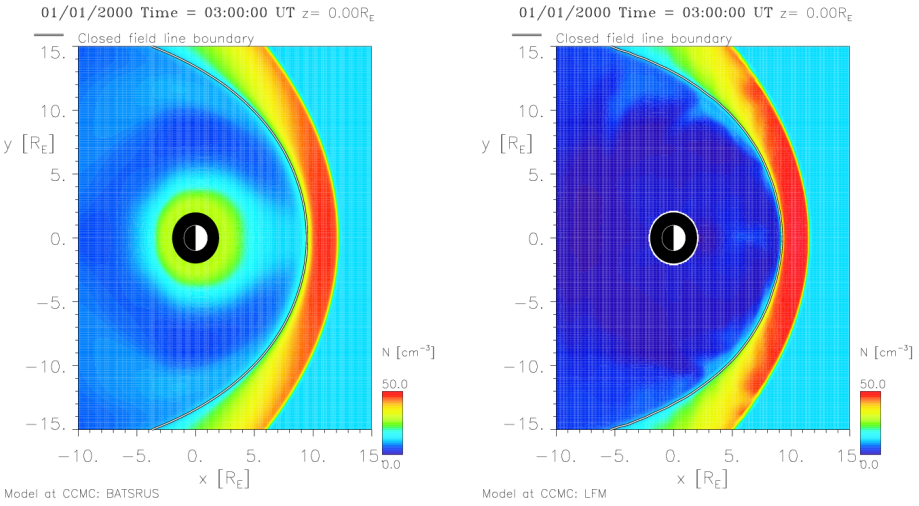

Figure 2. Density in the equatorial plane in the SWMF (left) and LFM (right) models in Case 1. The grey line indicates the position of the open-close field line boundary (magnetopause on the dayside).

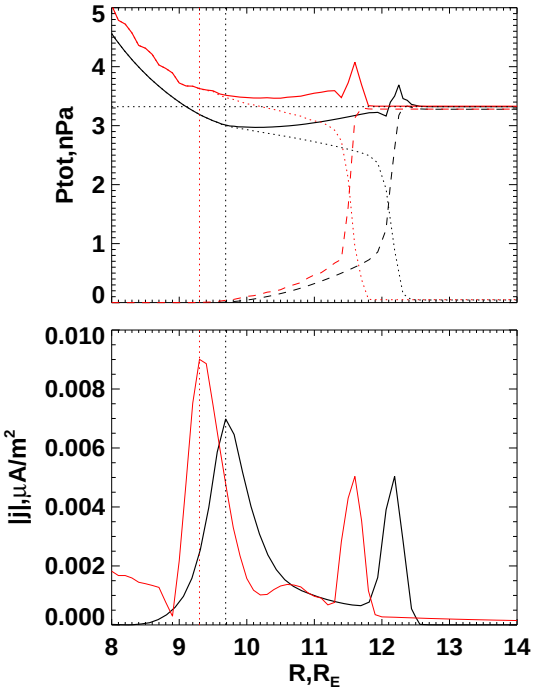

Figure 3. Top: dashed lines indicate dynamic pressure, dotted lines – the sum of thermal and magnetic pressures, solid lines – the sum of dynamic, thermal, and magnetic pressures along the Sun-Earth line. Dotted horizontal line points out the total pressure upstream of the bow shock (the same for both models). Bottom: electric current density. The peaks in electric current density on the left-hand side of the bottom plot correspond to the magnetopause position and are marked with dotted vertical lines. The peaks on the right-hand side correspond to the bow shock. Black (red) lines show results of the SWMF (LFM) models.

down in the magnetosheath. On the contrary, the LFM model predicts a $\sim 8\%$ increase in the total pressure. Then, the total pressure in both models slightly decreases through the magnetosheath. The dotted vertical lines mark the maxima of the electric current density which usually indicate the magnetopause position. In the SWMF model, the $|j|$ maximum is located at $x = 9.7\ R_E$ while it is shifted 0.4 R_E Earthward in the LFM model. For comparison, the empirical models predict the magnetopause at $x = 9.6\ R_E$ (Shue et al., 1998) and $x = 9.5\ R_E$ (Lin et al., 2010) in this particular case, in good agreement with the MHD simulations.

We only point out the difference in the magnetopause position between the models in this paper, but we do not study in detail the reasons for this difference. We suppose that the possible explanation might reside in the different numerical methods in the two models or different simulations in the inner magnetosphere and different inner boundary conditions.

3.2 Case 2

We present the MHD results in the four selected times in this case. Table 1 displays the key solar wind parameters (top panel) at 19:50, 22:15, 23:00, and 23:50 UT, the magnetospheric dipole tilt, and the magnetopause standoff distances in the empirical (Shue et al., 1998; Lin et al., 2010) and MHD SWMF and LFM models (bottom panel) taking into account the corresponding time lags between the solar wind boundary and magnetopause for the MHD models (5 min for the LFM model and 10 min for the SWMF model).

The solar wind density is higher than the average at 19:50 UT, while the velocity and magnetic field magnitude are close to typical values. Therefore the magnetosphere is only moderately compressed. Next, at t=22:15 UT, the solar wind density becomes extremely high and the magnetosphere is tremendously compressed, therefore the empirical Lin et al. (2010) model and both MHD models predict the standoff distance well inside geostationary orbit, at 6.1 or 5.8 R_E, even for the northward IMF. The Shue et al. (1998) model, however, predicts the standoff distance of 6.7 R_E, i.e. slightly higher than geostationary orbit at 6.6 R_E.

The solar wind density abruptly drops between 22:48 and 22:50 UT resulting in the magnetospheric expansion from 5.8 R_E at 22:50 UT to 7.4 R_E at 23:05 UT in the SWMF simulation. However, even at 23:00 and 23:50 UT all the solar wind parameters presented in Table 1 (density, velocity, IMF B_Z) are higher than those in the ordinary conditions, therefore the magnetosphere stays significantly compressed.

The empirical and MHD models predict different standoff distances and the differences between the models change in time. Although both empirical magnetopause models depend on the same solar wind conditions, they apply different power laws between the solar wind dynamic pressure and the standoff distance so that the variations of the standoff distance during magnetospheric compression are larger in the Lin et al. (2010) model than in the Shue et al. (1998) model. Besides, the Lin et al. (2010) model takes into account the dipole tilt, while the Shue et al. (1998) model does not. Moreover, the magnetopause standoff distance in the Lin et al. (2010) model depends on the sum of the solar wind dynamic and magnetic pressures while it depends only on the dynamic pressure in the Shue et al. (1998) model (but note that the magnetic pressure is usually one order of magnitude less than the dynamic pressure).

The SWMF model predicts the magnetopause to be closer to the Earth than both the empirical models for the compressed magnetospheric conditions. We refer to the paper of Samsonov et al. (2016) in which reasons for the differences between empirical and MHD models were discussed. Both empirical and MHD models might be inaccurate. Since empirical models are statistical, they may smooth standoff distance variations both for

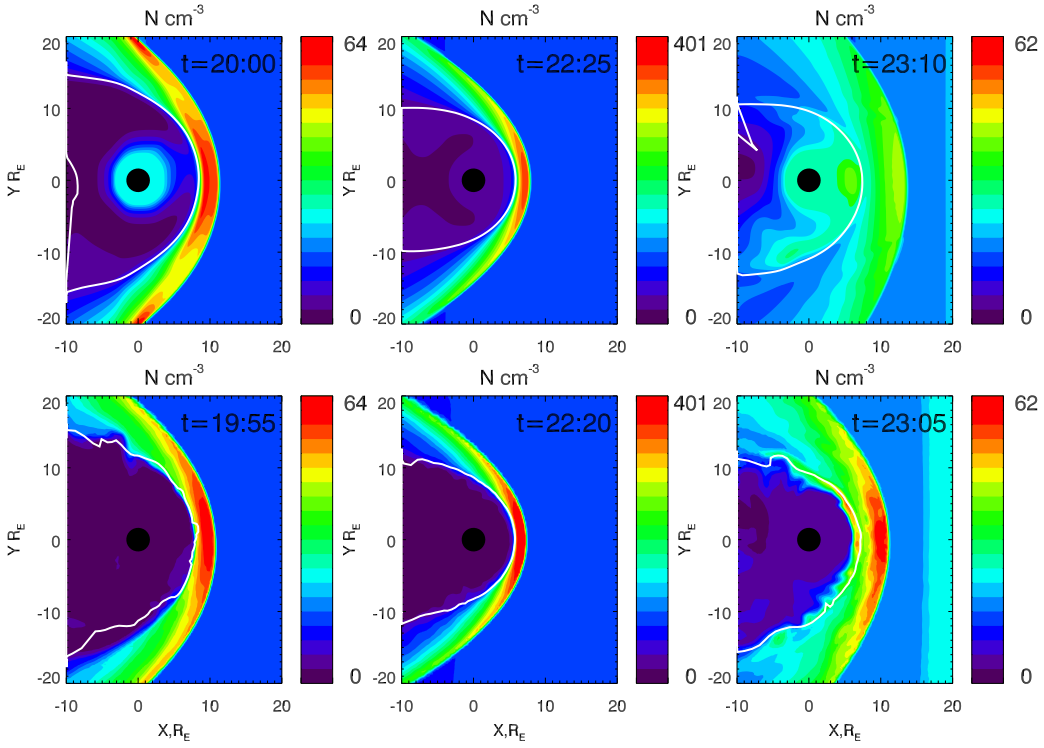

Figure 4. Density in the equatorial plane in the SWMF (top) and LFM (bottom) models in Case 2 at different times. The thick grey line indicates the open-closed field line boundary.

strong compressions and expansions. Besides, the empirical models depend only on present solar wind conditions, while the standoff distance in the MHD models smoothly evolves and therefore depends on the present and past conditions. On the other hand, MHD models may not accurately reproduce some magnetospheric currents, e.g., the ring current or the magnetospheric-ionospheric currents. Moreover, the present case occurs at a large dipole tilt, which exacerbates the differences between the models.

Figure 4 compares the density distribution in the equatorial plane at three times calculated by either the SWMF (top row) and LFM (bottom row) models. As mentioned above, we apply the additional time lag of 5 min between the SWMF and LFM simulations to obtain a better match of the density distribution in the magnetosheath and solar wind. Since the LFM model is less diffusive it can better reproduce some sharp density peaks observed by Wind and respectively the density maxima in the magnetosheath are sometimes higher (e.g., in the subsolar region downstream of the bow shock at t=23:05 UT).

At 20:00 (19:55 for LFM) UT, the magnetosphere is moderately compressed. The solar wind plasma parameters vary slowly, the IMF Bz is weak and positive, therefore the magnetopause position is stable. As well as in Case 1, the LFM model predicts a magnetospheric density lower than that in the magnetosheath and solar wind, while the SWMF model predicts a magnetospheric density close to or even higher than that in the solar wind and on the magnetosheath flanks. The density gradually decreases from 64 cm^{-3} in the subsolar magnetosheath at $x = 9.4\ R_E$ to 9.3 cm^{-3} in the magnetosphere at $x = 7.5\ R_E$ in the SWMF model. The LFM models predicts nearly the same density in the magnetosheath, but the density falls below 0.1 cm^{-3} in the subsolar magnetosphere at $x < 7\ R_E$.

The magnetosphere is extremely compressed at 22:25 (22:20 in the LFM model) UT with maximum densities of ∼400 cm^{-3} in the magnetosheath and corresponding solar wind densities of ∼100 cm^{-3}. The density in the outer magnetosphere in the SWMF simulation is also higher than that in quieter conditions even if it keeps the same at the inner boundary of the MHD domain. However, the density significantly drops through the magnetopause, e.g., from 340 cm^{-3} at x=6.6 R_E to 73 cm^{-3} at x=5.4 R_E, which forms a sharp boundary in Figure 4. In the LFM model, the density still stays fairly low in the magnetosphere varying from several cm^{-3} near the magnetopause to about 0.1 cm^{-3} near the inner boundary despite the huge magnetosheath density.

The density distribution at 23:10 (23:05) UT is essentially different from that we usually obtain in MHD simulations. The thick grey line that indicates the open-closed boundary (OCB) usually nearly coincides with the maximal density gradient at the magnetopause, except in this particular case. Interestingly, the SWMF model predicts an increase in the density through the inward OCB crossing, in particular from 27 cm^{-3} at x=8.0 R_E in the magnetosheath to 40 cm^{-3} at x=6.5 R_E in the outer magnetosphere. The magnetospheric density distribution is asymmetric with a higher density on the dawn side. In the LFM model, the sharp density gradient is located about 1 R_E Earthward of the OCB which demonstrates specifics of the density distribution at this time as well. Nevertheless, the magnetospheric density in the LFM simulation gradually decreases toward the Earth and stays below 1 cm^{-3} for $x < 5.5$ R_E.

Summarizing the comparison between the two MHD models, we conclude that the density in the magnetosphere predicted by the SWMF model is significantly higher than that predicted by the LFM model. Spacecraft observations mostly agree with the predictions of the LFM model, i.e. the density is low, e.g. about 1 cm^{-3}, in the dayside magnetosphere outside the plasmasphere (but it might be possible that particle detectors underestimate the cold ion density under certain conditions (Toledo-Redondo et al., 2019)). Consequently, we should reduce the density in the magnetosphere predicted by the SWMF model to zero or to very small values while simulating X-ray images. In the next section, we describe methods of magnetospheric masking which help us separate the magnetospheric and magnetosheath regions. On the other hand, we can simulate X-ray images for the LFM model without magnetospheric masking. We discuss this topic in detail below.

4 Magnetopause position and magnetospheric masking

4.1 Magnetopause position indicated by maximum of electric current density

The magnetopause is by definition a boundary between the magnetospheric and magnetosheath (i.e. solar wind connected) magnetic fields and consequently should coincide with a current layer which separates those fields. Samsonov et al. (2016) presented MHD simulations for stationary solar wind conditions with typical plasma and magnetic field parameters which illustrate that the maximum of electric current density J well indicates the magnetopause position in the dayside region. Figure 5 displays the electric current density in the equatorial and noon-meridional planes in Case 1. Although this is a stationary case with the purely northward IMF, the position of the subsolar magnetopause nearly coincides with the maximum of the electric current density as it occurs for other IMF orientations too. More precisely, the maximum of the current density is slightly farther from the Earth than the OCB indicated by thick white lines in Figure 5. Anyway, the electric current density can be used as a good indicator of the magnetopause position in the dayside region. The picture becomes more complicated near the cusps where simultaneously as many as three local maxima of the electric current density at different radial distances may appear (see right panel of Figure 5). Finding the magnetopause position becomes ambiguous in this case.

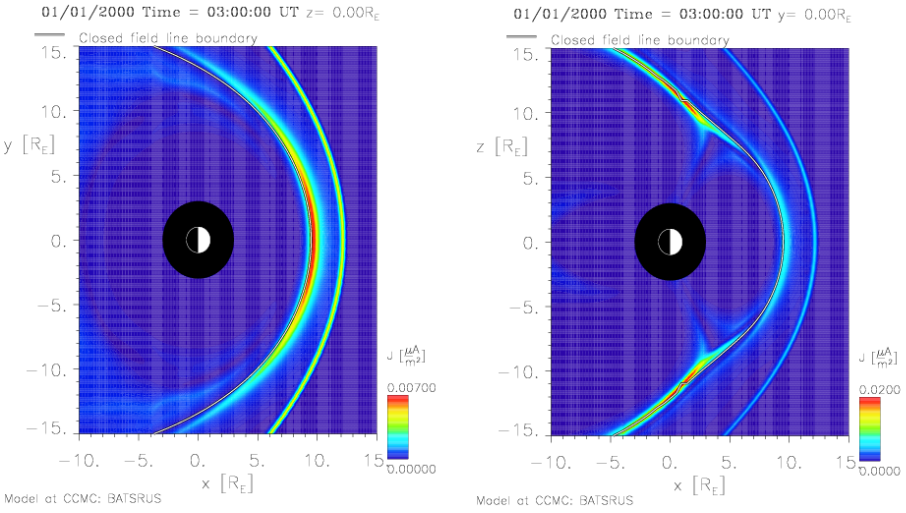

Figure 5. Electric current density in the equatorial (left) and noon-meridional(right) planes in the SWMF model in Case 1. Thick white line indicates the OCB.

While the electric current density in stationary MHD solutions usually has only two maxima in the subsolar region, one corresponding to the magnetopause and another one, farther from the Earth, indicating the bow shock, the picture may become more confusing in some non-stationary solutions. If a directional discontinuity (whether rotational or tangential, but with significant changes in the IMF orientation) or an interplanetary shock propagates through the magnetosheath, this results in another maximum of the electric current density which might be confused with the maximum at the magnetopause. An example of such temporal variations of J at t=23:00 UT in Case 2 is presented in Figure 6. The electric current layer in the middle of the magnetosheath, between the magnetopause and bow shock, corresponds to the tangential discontinuity with decreases in the density and IMF B_y and increase in the IMF B_z imposed at the upstream numerical boundary at about 22:49 UT. Such transient structures may cause problems for automatic identification of the magnetopause position in MHD simulations using electric current distributions. Fortunately, events with such strong directional discontinuities or interplanetary shocks are rare.

The inner local maximum of the electric current density along the Sun-Earth line always corresponds to the magnetopause even if more than two maxima of J between the magnetosphere and bow shock occur (as an exception a weak electric current layer might rapidly move through the dayside magnetosphere after impact of interplanetary shocks (Samsonov & Sibeck, 2013)). Figure 7 shows profiles of J along the Sun-Earth line in Case 1 and at several times in Case 2. The inner maximum at the magnetopause is highest in Case 1 and at 20:00 and 22:25 in Case 2. The maxima at the bow shock are highest at the three other times, so even at 23:00 the maximum in the middle of the magnetosheath does not exceed that at the bow shock. The inner maximum coincides with the magnetopause position in all cases.

4.2 Magnetospheric masking using threshold conditions

Usually MHD parameters in the dayside magnetosphere noticeably differ from those in the dayside magnetosheath. For example, the magnetospheric density and thermal pressure are lower, the flow velocity is lower as well, the magnetic field magnitude in the magnetosphere is typically larger but this depends on the IMF orientation since for a

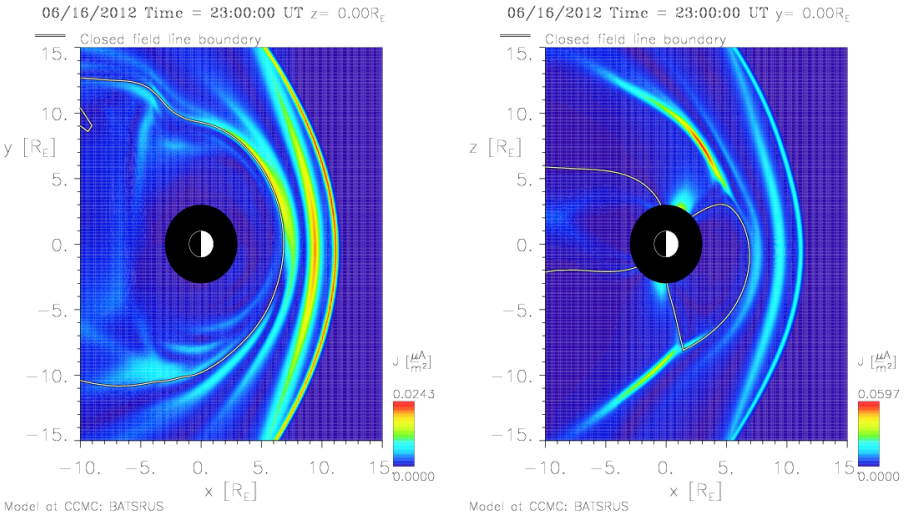

Figure 6. Electric current density in the equatorial (left) and noon-meridional(right) planes in the SWMF model at t=23:00 UT in Case 2. Thick white line indicates the OCB.

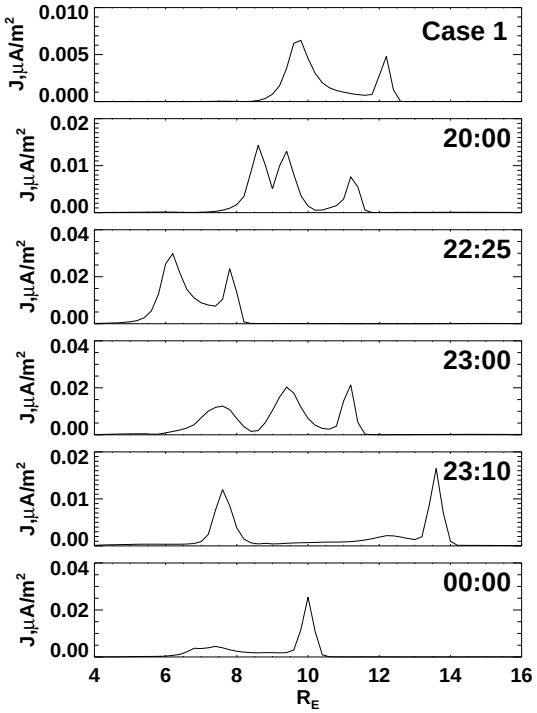

Figure 7. Electric current density along the Sun-Earth line in Case 1 and at different times in Case 2.

northward IMF the difference through the subsolar magnetopause may be small. However, the boundary layer between the magnetospheric and magnetosheath parameters is usually diffuse in MHD simulations and the magnetopause position sometimes can not be accurately determined. For example, the velocity decreases to zero at the stagnation point near the stationary subsolar magnetopause (Spreiter et al., 1966), however, the velocity may considerably increase both in the magnetosheath and in the outer magnetosphere on the flanks, near and behind the terminator plane (since the flowpause, the boundary between different streams, may not coincide with the magnetopause there). Therefore the velocity distribution alone cannot be used as a confident magnetopause indicator in the whole dayside region. Instead, we try several combinations of the different MHD parameters and describe a more reliable method below.

In Figure 8 a-b, we show that the thermal pressure is usually higher in the dayside magnetosheath and cusps than in both the magnetosphere and solar wind. However, the difference is blurred on the magnetosheath flanks, and therefore we apply additionally the second condition on velocity in the whole numerical box. We begin by finding the subsolar magnetopause position (e.g., using the electric current density profile at the Sun–Earth line), move $\sim 0.5\ R_E$ inward from it, and use the thermal pressure from this point for the first threshold condition. This point is supposed to be inside the magnetosphere, but close to the magnetopause. The threshold for the velocity is obtained far upstream of the bow shock, e.g. near the upstream numerical boundary. Thus we impose the following conditions to determine the magnetospheric area

$$\begin{aligned} p &< p(msp) + \Delta p, \\ V_X &> V_X(sw) * k_v. \end{aligned} \tag{2}$$

Here, $p(msp)$ and $V_X(sw)$ are the thresholds of the thermal pressure in the magnetosphere and the x component of the velocity in the solar wind respectively. Note that the latter is negative in the solar wind therefore V_X can be either small negative or positive in the magnetosphere. We set $\Delta p = 0.2$ nPa, and $k_v = 0.15$. If both conditions (2) are matched, the location is taken to be in the magnetosphere. We have tested more than ten MHD solutions with different solar wind conditions and this method mostly works well, however it may fail in some cases with highly variable solar wind conditions. We present both successful and failed examples below.

Figure 8 shows the thermal pressure (a,b) and X-ray emissivity (c,d) (see equation (1)) in the equatorial and noon-meridional planes in case 1 calculated by using the SWMF model and applying the magnetospheric mask. Note that we use the logarithmic scale for the emissivity plots in this figure and below. The magnetosheath and cusps are evident in the 2-D slices of thermal pressure. The region of highest pressure is the subsolar magnetosheath. The thermal pressure in the cusps and on the magnetosheath flanks is lower, but still larger than that in the magnetosphere. Such pressure distribution is typical for MHD simulations (particularly for those cases with steady or slowly changing solar wind conditions) and the magnetospheric masking method using conditions (2) well separates the magnetosheath and cusps from the solar wind and magnetosphere in such cases. We obtain that the emissivity in the cusps is several times higher than that in the subsolar magnetosheath, e.g. the maximum P_X in the cusp in the noon-meridional plane reaches $9.8 \cdot 10^{-5}$ eV cm^{-3} s^{-1} while the maximum P_X in the subsolar magnetosheath in the equatorial plane is only $2.5{\cdot}10^{-5}$ eV cm^{-3} s^{-1}. We use logarithmic color scales for the following emissivity plots to better illustrate this difference. Figure 8 (e,f) shows the emissivity in the same case calculated without the magnetospheric mask. We can not confidently determine the magnetopause position in this case.

However, MHD models sometimes predict a relatively high thermal pressure in the magnetosphere, nearly the same or higher than that in the cusps and magnetosheath.

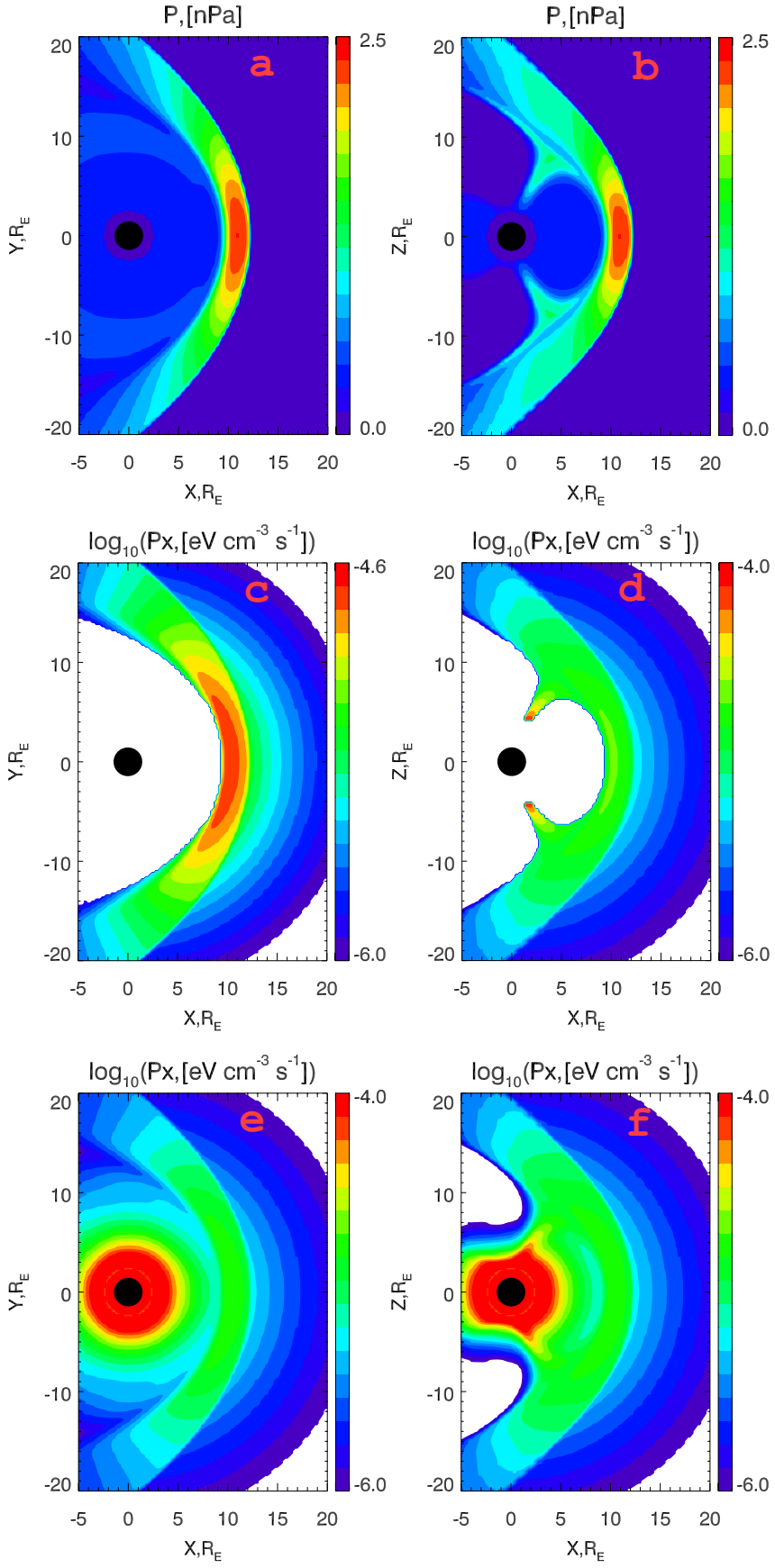

Figure 8. Thermal pressure (a,b) and X-ray emissivity calculated with the masking based on conditions (2) (c,d) in the equatorial (a,c) and noon-meridional (b,d) planes in Case 1. Panels (e,f) show the emissivity for the same case without magnetospheric mask.

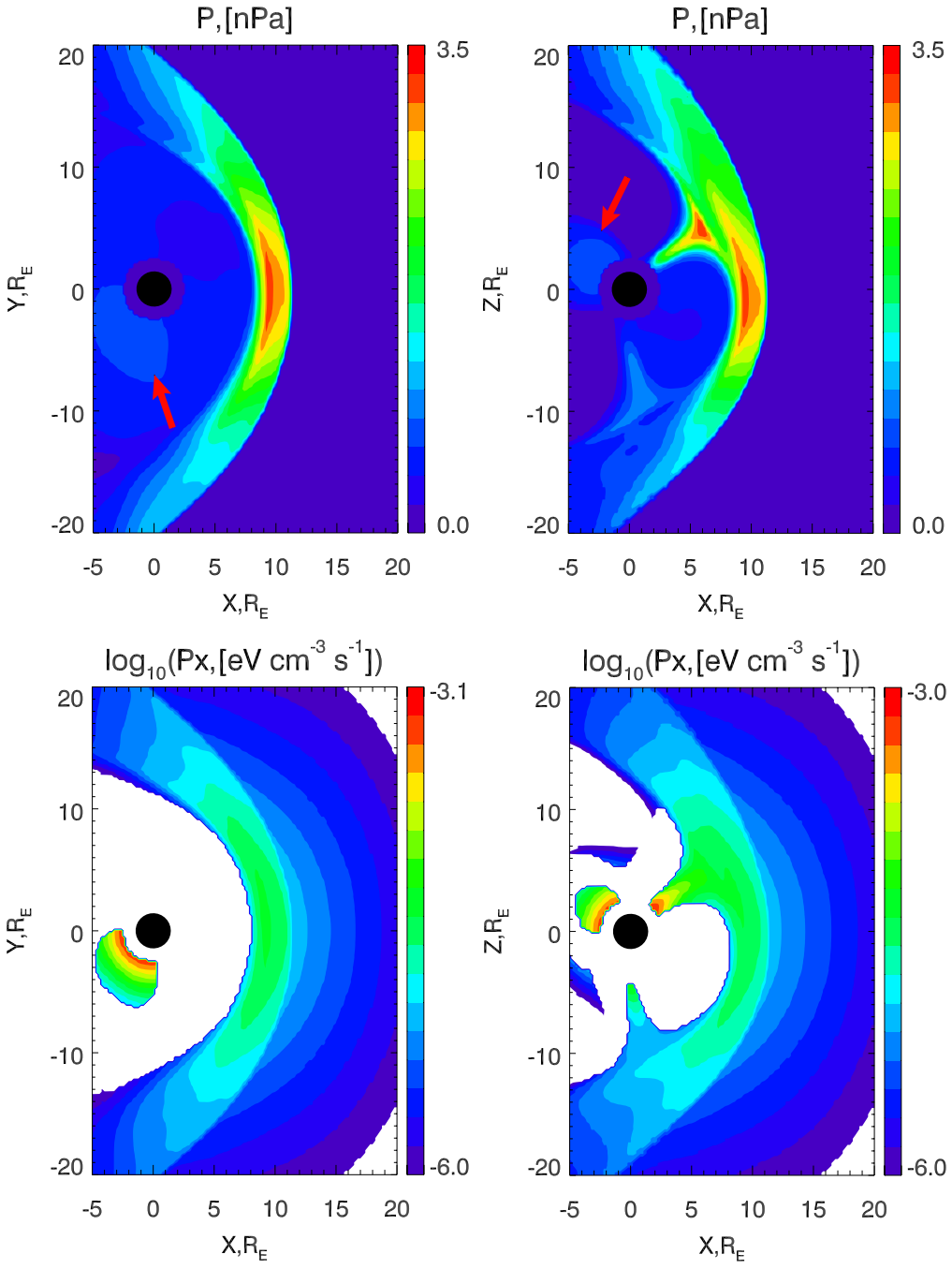

Figure 9. Thermal pressure (top) and emissivity (bottom) in the equatorial and noon-meridional planes in Case 2 at 20:00 UT (16 July) for the non-coupled SWMF model. Red arrows indicate the region in which the thermal pressure is higher than the average in the magnetosphere and close to that in the southern cusp and flank magnetosheath.

We have found several such examples in the simulations of Case 2. Figure 9 shows the thermal pressure and X-ray emissivity in the same format as in Figure 8 (a-d), but at 20:00 UT on 16 June, 2012. At first glance, the thermal pressure in the magnetosphere seems to be lower than that in the magnetosheath. However, the dipole is strongly tilted in this case which results in a large north-south asymmetry. The pressure in the northern cusp is several times higher than that in the southern cusp. Moreover, the magnetopause shape and pressure distribution in the magnetosheath is also asymmetric. At the same time, there are regions in the magnetosphere where the pressure is higher than the average and reaches about the same values as in the southern cusp and flank magnetosheath. This occurs in the nightside region on closed field lines near the Earth and is visible in the noon-midnight plane as well as on the dawn side in the equatorial plane (the two regions indicated by red arrows in Figure 9). As a result, the masking method with pressure thresholds is not able to separate the whole magnetospheric domain from the cusps and flank magnetosheath. In this case, we obtain that some regions in the nightside magnetosphere do not match the masking condition (2). This results in a high X-ray emissivity in several spots in the inner magnetospheric region which we do not expect to be a source of X-rays in reality. However, this will not be a problem in our study because we concentrate on the emissivity in the dayside region.

Note that the pressure distribution in the magnetosphere may change while using a global MHD model coupled with kinetic models developed for the inner magnetosphere, like the Rice Convection Model (RCM). The results shown in Figure 9 were obtained for the non-coupled SWMF code. Figure 10 shows the simulations at the same time for the SWMF coupled with RCM. In this case, the growth of the thermal pressure in the inner magnetosphere is larger than in the simulations by the non-coupled SWMF model, and the size of the regions of the enhanced pressure is also bigger. This displays the way in which the RCM influences the results of MHD simulations, namely it changes the pressure distribution in the magnetosphere. As a result, the pressure threshold condition fails even in a larger magnetospheric zone therefore the size of the high X-ray emissivity region in the inner magnetosphere is larger there than for the non-coupled SWMF model. We believe that this is a flaw of our masking method because we do not expect that high-charge state solar wind ions can penetrate into the inner magnetosphere.

4.3 Magnetospheric masking using flowlines

We find that the method of magnetospheric masking using thermal pressure thresholds can fail in cases with high pressure zones in the magnetosphere, therefore another method is presented in this subsection. In this method, every grid point in the simulation box is traced back along its flowline until the flowline reaches the supersonic solar wind. If the flowline does not reach the supersonic solar wind in a reasonable time, then this point is taken to be in the magnetosphere. Sun et al. (2019) also used the flowline method for magnetospheric masking, but their algorithm was different and implied using a numerical code to solve the continuity equation. In our method, we need only a 3-D velocity distribution and a relatively simple code to calculate the motion along flowlines. We further reduce the computational time by making a preliminary separation of grid points, i.e. points with $|V| > 0.65V_{SW}$ are assumed to be related to the solar wind (they could be in the supersonic solar wind, magnetosheath, or far magnetotail) and points with $|V| < 0.01V_{SW}$ are assumed to be in the magnetosphere. Then we trace the remaining points until one of the two conditions above is fulfilled.

The flowlines traced back to the solar wind outline the dayside magnetosphere, but they do not mark the cusps. It means that the cusps are determined as magnetospheric regions despite the fact that the solar wind plasma fills the cusps in observations. We apply the method suggested by Sun et al. (2019) to mark the cusps. In this method, we make two local spherical grids separately for the northern and southern hemispheres for the interval of radial distances which cover the expected cusp locations. The grid spac-

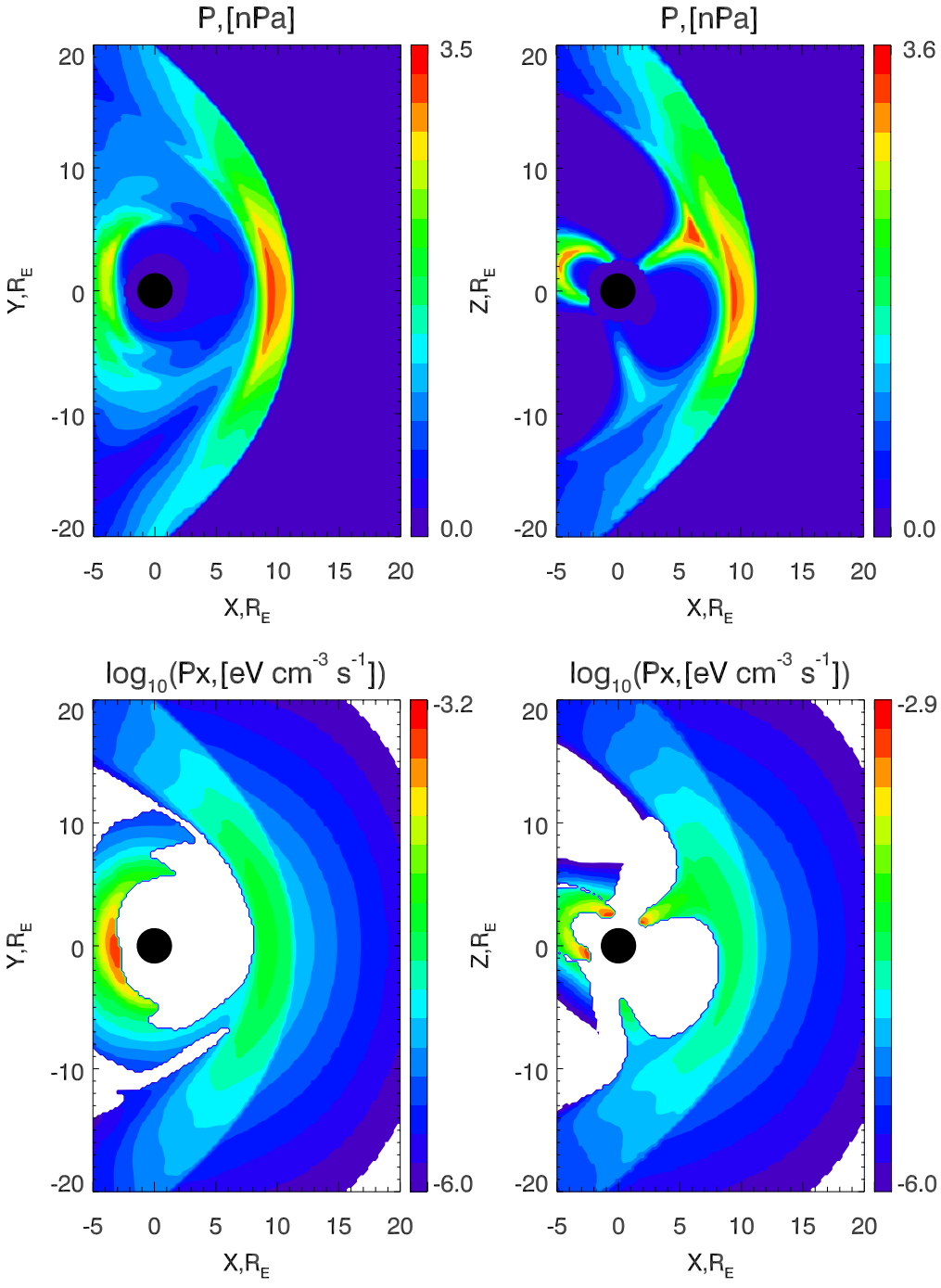

Figure 10. Thermal pressure (top) and emissivity (bottom) in the equatorial and noon-meridional planes in Case 2 at 20:00 UT for the SWMF coupled with RCM. The region of high thermal pressure is located in the nightside magnetosphere. Correspondingly, the magnetospheric mask does not cover this region, and we obtain a large X-ray emissivity there.

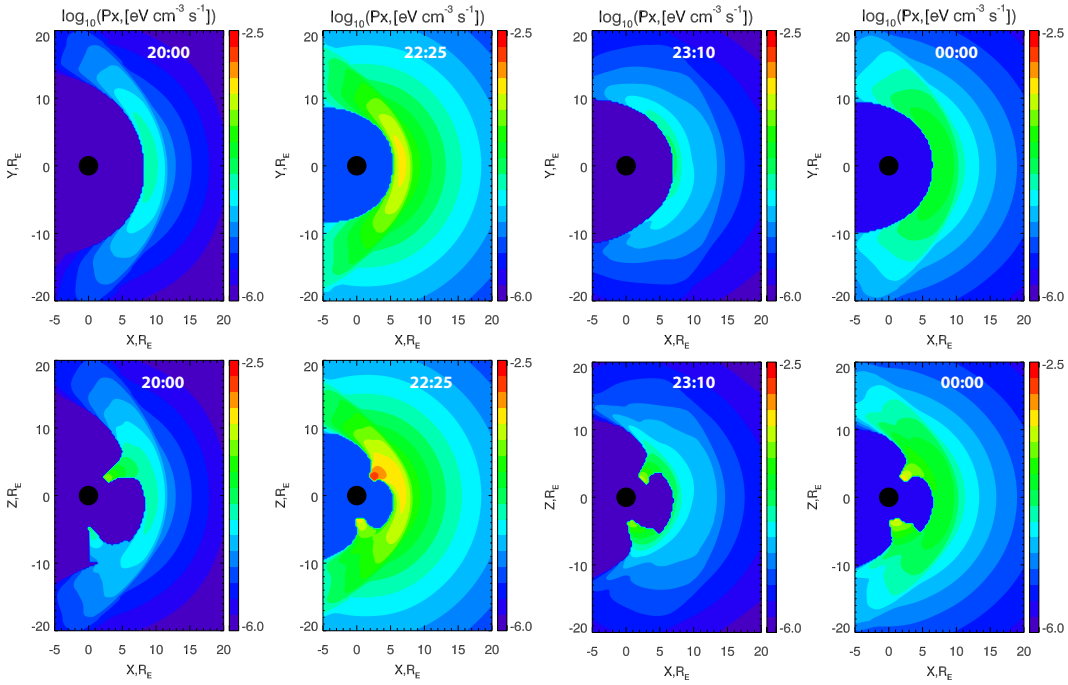

Figure 11. Emissivity in the equatorial and noon-meridional planes in Case 2 at 20:00, 22:25, and 23:10 UT on 16 June and at 00:00 on 17 June calculated by the masking method with flowlines.

ing in radial direction is 0.125 R_E. For each radial shell, we find the maximum of the plasma pressure p_{max} and select a surrounding zone of the high pressure using condition $p > k_p p_{max}$ where $k_p = 0.7$. We inspected several k_p values and found that the difference in the selected area for different k_p is negligible for stationary cases without a dipole tilt, such as case 1, but it might become significant for real events with a large dipole tilt, such as case 2. We choose a value of k_p which provides a smoothest transition at the outer boundary of the cusps.

Figure 11 shows the X-ray emissivity at 20:00, 22:25, and 23:10 UT on 16 June and at 00:00 on 17 June in case 2 calculated by using the magnetospheric masking method with flowlines. The dipole tilt results in the north-south asymmetry in all cases. The emissivity is generally higher in the northern cusp where the solar wind density is higher too. The flowline masking method provides a smooth boundary which clearly separates the magnetosphere from the cusps and magnetosheath. The outer boundary of the magnetosphere in the subsolar region determined by the flowline masking method generally nearly coincides with the open-closed field line boundary except in several extreme cases.

In Figure 12, we show profiles of the emissivity, density, and electric current density along the Sun-Earth line at four times for Case 2. Firstly, the figure illustrates that the maximum of the emissivity near the subsolar magnetopause differs by more than one order of magnitude at different times depending on the magnetospheric compression (Px maximum located in the northern cusp is weakest at 20:00 UT and strongest at 22:25 UT). Secondly, positions of the maximum of emissivity, the maximum density gradient, and the maximum of the electric current density change relative to each other at different times. At 20:00 and 22:25 UT, when the solar wind conditions are relatively stable, the positions of the maximum of density gradient and the maximum of electric current density nearly coincide with each other. Note that the grid spacing is 0.25 R_E in this run. The density and electric current density are taken at the centers of the numerical

grid cells, while the density gradient is taken at the boundaries between the cells which results in the 0.125 R_E difference. The position of the emissivity maximum is located 0.25-0.5 R_E sunward of the electric current (or density gradient) maximum. At 23:10 UT, immediately after a significant drop of the solar wind density, the magnetosphere rapidly expands and the simulation predicts density in the closed field line region (i.e. in the magnetosphere) larger than that in the inner part of the magnetosheath. Therefore the maximum of the density gradient $grad(N)$ is shifted about 2 R_E earthward of the maximum of electric current density j which indicates the magnetopause current layer. The emissivity maximum and the flowline boundary (i.e., a sharp drop of the emissivity) are located between the maxima of $grad(N)$ and $|j|$. At 00:00 UT, the solar wind conditions are relatively stable but the magnetospheric density remains rather high. Therefore the emissivity maximum again nearly coincides with the flowline boundary and is located earthward of the maxima of $grad(N)$ and $|j|$.

4.4 Emissivity in LFM model

As noted above, the LFM model predicts a small magnetospheric density, below 1 cm^{-3}, therefore we can use the X-ray emissivity without magnetospheric masks for simulation of SXI images. In Figure 13, we compare the emissivity obtained without (left panels) and with (right panels) magnetospheric masking at 20:00 and 22:25 UT. The magnetospheric mask has been constructed using the threshold conditions in equation (2). As in the case of the SWMF model, the emissivity close to the Earth in the simulation without masking may be significantly larger than in the magnetosheath because of the extremely high neutral density (since the neutral density is proportional to R^{-3}). However, contrary to the results obtained from the SWMF model, the LFM model predicts the emissivity in the dayside magnetosphere to be smaller than that in the magnetosheath and therefore we can distinguish the magnetopause position (e.g., see upper left panel at 20:00 UT). In the case of extreme magnetospheric compression at 22:25 UT, the magnetopause position in the simulation without a mask cannot be precisely determined because the decrease in the solar wind density through the magnetopause in the MHD results is mostly compensated by the large increase in the neutral density. In most other cases, the predicted emissivity in the LFM model looks similar to the results at 20:00 UT and therefore the simulations of SXI images can proceed without magnetospheric masks.

5 Conclusions

The energy transfer rate from the solar wind into the magnetosphere can be characterized by combinations of the solar wind parameters (e.g., Perreault & Akasofu, 1978; Vasyliunas et al., 1982; Newell et al., 2007, and references therein). The magnetospheric state can also be presented by combinations of several global parameters, e.g. by the auroral indices SML/SMU (from the SUPERMAG network (Gjerloev, 2012)) or the traditional AL/AU, the ring current index SMR or Dst, the cross polar cap potential, the size of the polar cap, and so on. The magnetopause standoff distance may also be included in this list because it characterizes global magnetospheric compressions and expansions. The magnetopause location and motion provide crucial information concerning the state of the solar wind magnetosphere interaction, in particular the reconnection rate and the amount of flux transferred from the dayside to the magnetotail and vice-versa. Up to now, we have been unable to measure the standoff distance directly. In-situ spacecraft observations provide magnetopause crossings at some distance from the subsolar point and reveal a momentary magnetopause distance or distances during brief intervals in the case of multiple magnetopause crossings. The standoff distance is often included in empirical magnetopause models, but these models are averaged over many events and solar wind conditions without taking into account time dependence and often assume a predefined functional form to describe the magnetopause shape. The new space

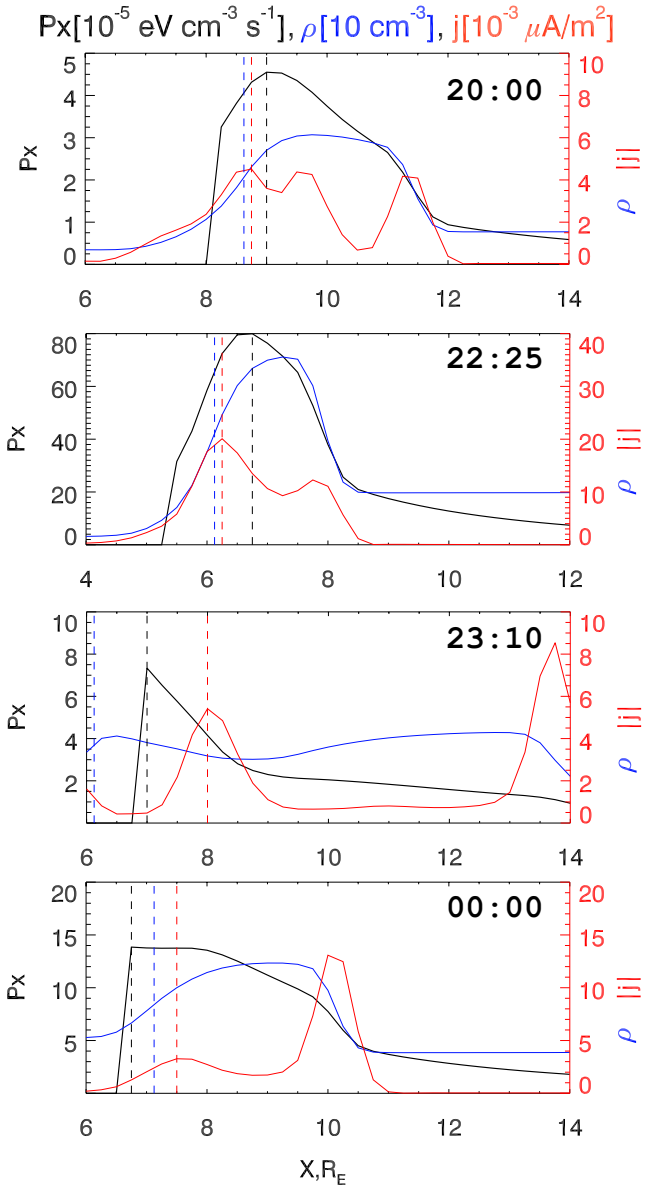

Figure 12. Emissivity (black), density (blue), and electric current density (red) along the Sun-Earth line at different times (20:00, 22:25, 23:10, and 00:00 UT). Dashed vertical lines indicate maxima of the emissivity (black), maxima of the density gradient (blue), and maxima of the electric current density at the magnetopause (red).

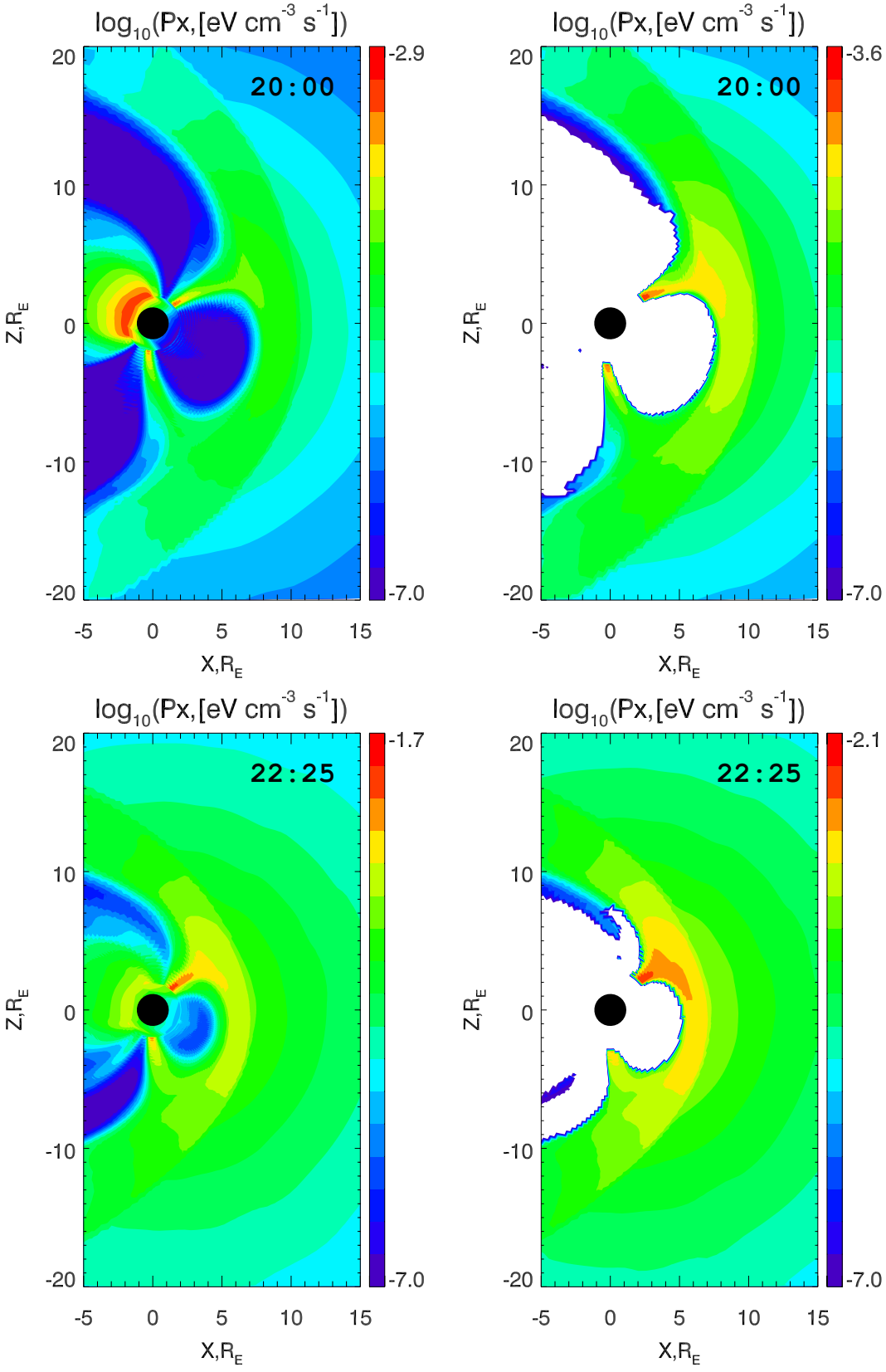

Figure 13. Emissivity in the noon-meridional planes in Case 2 at 20:00 and 22:25 UT without a magnetospheric mask (left) and with the mask obtained from threshold conditions (right) for numerical results of the LFM model.

mission SMILE will observe X-rays emitted in the magnetosheath and cusps capturing temporal variations of the magnetopause standoff distance in response to solar wind variations.

This paper is the first of two companion papers in which we discuss the methods of finding the magnetopause positions using soft X-ray images. We use the two global MHD models, SWMF and LFM, and simulate one artificial and one real event. We briefly discuss the reasons why the numerical models predict different magnetopause positions for the same solar wind conditions. We illustrate how significantly the density distribution in the magnetosphere and magnetopause position may change in response to large variations of the solar wind plasma parameters and magnetic field. We compare predictions of the MHD and empirical magnetopause models. We emphasize that the maximum electric current density is a good indicator of the magnetopause location even in a northward IMF case.

The density in the outer dayside magnetosphere predicted by the LFM model varies between 0.1 and 10 cm^{-3} depending on the magnetospheric compression. This generally agrees with observations. The SWMF model predicts the magnetospheric density between 10 and 50 cm^{-3} (the last in the case of strong compression). If we calculate the X-ray emissivity in this case, we cannot clearly distinguish the magnetopause position because the difference in the emissivity between the dayside magnetosphere and magnetosheath is too small. On the contrary, the magnetopause location can be found by using the emissivity distribution calculated by the LFM model, except for some specific cases with a fast magnetospheric expansion. We present the two methods of magnetospheric masking which separate the points located in the magnetosphere from those located in the magnetosheath, cusps, and solar wind. The first method uses threshold conditions for the thermal pressure and velocity, and the second method applies tracing along flowlines. Using these methods, we can calculate the X-ray emissivity localized in the magnetosheath and cusps. The results of the calculations are used in the second paper for simulation of 2-D X-ray images and SXI counts maps.

Acknowledgments

This work was carried out using the SWMF/BATSRUS tools developed at The University of Michigan Center for Space Environment Modeling and the LFM–MIX magnetosphere-ionosphere model developed at Dartmouth College/High Altitude Observatory/Johns Hopkins University Applied Physics Laboratory/Center for Integrated Space Weather Modeling available through the NASA Community Coordinated Modeling Center (http://ccmc.gsfc.nasa.gov). In particular, we used results of the runs *Andrei_Samsonov_080818_2*, *Andrei_Samsonov_083118_1*, *Andrei_Samsonov_021819_1*, *Andrey_Samsonov_070519_1*, and *Andrey_Samsonov_073119_1*.

AAS and GBR acknowledge support from the UK Space Agency under grant ST/T002964/1. AAS work is also partly supported by the International Space Science Institute (ISSI). JAC is supported by the Royal Society Dorothy Hodgkin Fellowship.

References

Archer, M., Turner, D., Eastwood, J., Schwartz, S., & Horbury, T. (2015). Global impacts of a foreshock bubble: Magnetosheath, magnetopause and ground-based observations. *Planetary and Space Science*, *106*, 56-66. Retrieved from `https://www.sciencedirect.com/science/article/pii/S0032063314003900` doi: https://doi.org/10.1016/j.pss.2014.11.026

Branduardi-Raymont, G., Sembay, S. F., Eastwood, J. P., Sibeck, D. G., Abbey, T. A., Brown, P., ... Yeoman, T. K. (2012, April). Axiom: advanced x-ray imaging of the magnetosphere. *Experimental Astronomy*, *33*(2-3), 403-443.

629 doi: 10.1007/s10686-011-9239-0

630 Branduardi-Raymont, G., Wang, C., & Escoubet, C. P. e. a. (2018). *Smile defi-*
631 *nition study report* (No. 1). European Space Agency, ESA/SCI. Retrieved
632 from https://sci.esa.int/web/smile/-/61194-smile-definition-study
633 -report-red-book

634 Carter, J. A., Milan, S. E., Fogg, A. R., Sangha, H., Lester, M., Paxton, L. J., &
635 Anderson, B. J. (2020). The evolution of long-duration cusp spot emis-
636 sion during lobe reconnection with respect to field-aligned currents. *Jour-*
637 *nal of Geophysical Research: Space Physics*, *125*(7), e2020JA027922. Re-
638 trieved from https://agupubs.onlinelibrary.wiley.com/doi/abs/
639 10.1029/2020JA027922 (e2020JA027922 10.1029/2020JA027922) doi:
640 10.1029/2020JA027922

641 Carter, J. A., Sembay, S., & Read, A. M. (2010, 02). A high charge state coro-
642 nal mass ejection seen through solar wind charge exchange emission as
643 detected by XMM-Newton. *Monthly Notices of the Royal Astronomical*
644 *Society*, *402*(2), 867-878. Retrieved from https://doi.org/10.1111/
645 j.1365-2966.2009.15985.x doi: 10.1111/j.1365-2966.2009.15985.x

646 Case, N. A., & Wild, J. A. (2013). The location of the earth's magnetopause:
647 A comparison of modeled position and in situ cluster data. *Journal of*
648 *Geophysical Research: Space Physics*, *118*(10), 6127-6135. Retrieved from
649 https://agupubs.onlinelibrary.wiley.com/doi/abs/10.1002/jgra.50572
650 doi: https://doi.org/10.1002/jgra.50572

651 Collier, M., Porter, F., Sibeck, D., Carter, J., Chiao, M., Chornay, D., ... Thomas,
652 N. (2012). Prototyping a global soft x-ray imaging instrument for heliophysics,
653 planetary science, and astrophysics science. *Astronomische Nachrichten*,
654 *333*(4), 378-382. Retrieved from https://onlinelibrary.wiley.com/doi/
655 abs/10.1002/asna.201211662 doi: https://doi.org/10.1002/asna.201211662

656 Collier, M. R., & Connor, H. K. (2018). Magnetopause surface reconstruc-
657 tion from tangent vector observations. *Journal of Geophysical Re-*
658 *search: Space Physics*, *123*(12), 10,189-10,199. Retrieved from https://
659 agupubs.onlinelibrary.wiley.com/doi/abs/10.1029/2018JA025763 doi:
660 https://doi.org/10.1029/2018JA025763

661 Cravens, T. E. (2000). Heliospheric x-ray emission associated with charge transfer
662 of the solar wind with interstellar neutrals. *The Astrophysical journal*, *532*(2),
663 L153-L156. doi: https://doi.org/10.1086/312574

664 Cravens, T. E., Robertson, I. P., & Snowden, S. L. (2001). Temporal vari-
665 ations of geocoronal and heliospheric x-ray emission associated with
666 the solar wind interaction with neutrals. *Journal of Geophysical Re-*
667 *search: Space Physics*, *106*(A11), 24883-24892. Retrieved from https://
668 agupubs.onlinelibrary.wiley.com/doi/abs/10.1029/2000JA000461 doi:
669 https://doi.org/10.1029/2000JA000461

670 Dmitriev, A. V., Lin, R. L., Liu, S. Q., & Suvorova, A. V. (2016). Model prediction
671 of geosynchronous magnetopause crossings. *Space Weather*, *14*(8), 530-543.
672 Retrieved from https://agupubs.onlinelibrary.wiley.com/doi/abs/
673 10.1002/2016SW001385 doi: https://doi.org/10.1002/2016SW001385

674 Dmitriev, A. V., & Suvorova, A. V. (2000). Three-dimensional artificial neural
675 network model of the dayside magnetopause. *Journal of Geophysical Re-*
676 *search: Space Physics*, *105*(A8), 18909-18918. Retrieved from https://
677 agupubs.onlinelibrary.wiley.com/doi/abs/10.1029/2000JA900008 doi:
678 https://doi.org/10.1029/2000JA900008

679 Gjerloev, J. W. (2012). The supermag data processing technique. *Journal of Geo-*
680 *physical Research: Space Physics*, *117*(A9). Retrieved from https://agupubs
681 .onlinelibrary.wiley.com/doi/abs/10.1029/2012JA017683 doi: 10.1029/
682 2012JA017683

683 Gordeev, E., Sergeev, V., Honkonen, I., Kuznetsova, M., Rastätter, L., Palmroth,

M., ... Wiltberger, M. (2015). Assessing the performance of community-available global mhd models using key system parameters and empirical relationships. *Space Weather*, *13*(12), 868-884. Retrieved from https://agupubs.onlinelibrary.wiley.com/doi/abs/10.1002/2015SW001307 doi: 10.1002/2015SW001307

Kuntz, K. D., Collado-Vega, Y. M., Collier, M. R., Connor, H. K., Cravens, T. E., Koutroumpa, D., ... Walsh, B. M. (2015, jul). The solar wind charge-exchange production factor for hydrogen. *The Astrophysical Journal*, *808*(2), 143. Retrieved from https://doi.org/10.1088/0004-637x/808/2/143 doi: 10.1088/0004-637x/808/2/143

Lin, R. L., Zhang, X. X., Liu, S. Q., Wang, Y. L., & Gong, J. C. (2010). A three-dimensional asymmetric magnetopause model. *Journal of Geophysical Research (Space Physics)*, *115*, A04207. doi: 10.1029/2009JA014235

Lyon, J. G., Fedder, J. A., & Mobarry, C. M. (2004, October). The lyon-fedder-mobarry (lfm) global mhd magnetospheric simulation code. *Journal of Atmospheric and Solar-Terrestrial Physics*, *66*, 1333-1350. doi: 10.1016/j.jastp.2004.03.020

Merkin, V. G., & Lyon, J. G. (2010). Effects of the low-latitude ionospheric boundary condition on the global magnetosphere. *Journal of Geophysical Research: Space Physics*, *115*(A10). doi: 10.1029/2010JA015461

Newell, P. T., Sotirelis, T., Liou, K., Meng, C.-I., & Rich, F. J. (2007). A nearly universal solar wind-magnetosphere coupling function inferred from 10 magnetospheric state variables. *Journal of Geophysical Research: Space Physics*, *112*(A1). Retrieved from https://agupubs.onlinelibrary.wiley.com/doi/abs/10.1029/2006JA012015 doi: 10.1029/2006JA012015

Pepino, R., Kharchenko, V., Dalgarno, A., & Lallement, R. (2004, dec). Spectra of the x-ray emission induced in the interaction between the solar wind and the heliospheric gas. *The Astrophysical Journal*, *617*(2), 1347–1352. Retrieved from https://doi.org/10.1086/425682 doi: 10.1086/425682

Perreault, P., & Akasofu, S. I. (1978, 09). A study of geomagnetic storms. *Geophysical Journal International*, *54*(3), 547-573. Retrieved from https://doi.org/10.1111/j.1365-246X.1978.tb05494.x doi: 10.1111/j.1365-246X.1978.tb05494.x

Petrinec, S. M., & Russell, C. T. (1996). Near-earth magnetotail shape and size as determined from the magnetopause flaring angle. *J. Geophys. Res.*, *101*, 137-152. doi: 10.1029/95JA02834

Powell, K. G., Roe, P. L., Linde, T. J., Gombosi, T. I., & De Zeeuw, D. L. (1999). A solution-adaptive upwind scheme for ideal magnetohydrodynamics. *Journal of Computational Physics*, *154*(2), 284 - 309. Retrieved from http://www.sciencedirect.com/science/article/pii/S002199919996299X doi: https://doi.org/10.1006/jcph.1999.6299

Ridley, A. J., Gombosi, T. I., & DeZeeuw, D. L. (2004). Ionospheric control of the magnetosphere: conductance. *Annales Geophysicae*, *22*(2), 567–584. Retrieved from https://angeo.copernicus.org/articles/22/567/2004/ doi: 10.5194/angeo-22-567-2004

Robertson, I. P., Collier, M. R., Cravens, T. E., & Fok, M.-C. (2006). X-ray emission from the terrestrial magnetosheath including the cusps. *Journal of Geophysical Research: Space Physics*, *111*(A12). Retrieved from https://agupubs.onlinelibrary.wiley.com/doi/abs/10.1029/2006JA011672 doi: https://doi.org/10.1029/2006JA011672

Samsonov, A. A., Gordeev, E., Tsyganenko, N. A., Šafránková, J., Němeček, Z., Šimunek, J., ... Raeder, J. (2016, July). Do we know the actual magnetopause position for typical solar wind conditions? *Journal of Geophysical Research (Space Physics)*, *121*, 6493-6508. doi: 10.1002/2016JA022471

Samsonov, A. A., Němeček, Z., Šafránková, J., & Jelínek, K. (2012). Why does

the subsolar magnetopause move sunward for radial interplanetary magnetic field? *Journal of Geophysical Research: Space Physics*, *117*(A5). Retrieved from https://agupubs.onlinelibrary.wiley.com/doi/abs/10.1029/2011JA017429 doi: 10.1029/2011JA017429

Samsonov, A. A., & Sibeck, D. G. (2013). Large-scale flow vortices following a magnetospheric sudden impulse. *Journal of Geophysical Research: Space Physics*, *118*(6), 3055-3064. Retrieved from https://agupubs.onlinelibrary.wiley.com/doi/abs/10.1002/jgra.50329 doi: https://doi.org/10.1002/jgra.50329

Samsonov, A. A., Sibeck, D. G., Dmitrieva, N. P., & Semenov, V. S. (2017). What happens before a southward imf turning reaches the magnetopause? *Geophysical Research Letters*, *44*(18), 9159-9166. Retrieved from https://agupubs.onlinelibrary.wiley.com/doi/abs/10.1002/2017GL075020 doi: https://doi.org/10.1002/2017GL075020

Samsonov, A. A., Sibeck, D. G., Dmitrieva, N. P., Semenov, V. S., Slivka, K. Y., Šafránková, J., & Němeček, Z. (2018). Magnetosheath propagation time of solar wind directional discontinuities. *Journal of Geophysical Research: Space Physics*, *123*(5), 3727-3741. Retrieved from https://agupubs.onlinelibrary.wiley.com/doi/abs/10.1029/2017JA025174 doi: 10.1029/2017JA025174

Shen, F., Shen, C., Zhang, J., Hess, P., Wang, Y., Feng, X., ... Yang, Y. (2014). Evolution of the 12 july 2012 cme from the sun to the earth: Data-constrained three-dimensional mhd simulations. *Journal of Geophysical Research: Space Physics*, *119*(9), 7128-7141. Retrieved from https://agupubs.onlinelibrary.wiley.com/doi/abs/10.1002/2014JA020365 doi: 10.1002/2014JA020365

Shue, J.-H., Song, P., Russell, C. T., Steinberg, J. T., Chao, J. K., Zastenker, G., ... Kawano, H. (1998). Magnetopause location under extreme solar wind conditions. *J. Geophys. Res.*, *103*, 17691-17700. doi: 10.1029/98JA01103

Sibeck, D. G., Allen, R., Aryan, H., Bodewits, D., Brandt, P., Branduardi-Raymont, G., ... Wing, S. (2018, June). Imaging Plasma Density Structures in the Soft X-Rays Generated by Solar Wind Charge Exchange with Neutrals. *Space Science Reviews*, *214*(4), 79. doi: 10.1007/s11214-018-0504-7

Sibeck, D. G., Lopez, R. E., & Roelof, E. C. (1991). Solar wind control of the magnetopause shape, location, and motion. *Journal of Geophysical Research: Space Physics*, *96*(A4), 5489-5495. doi: 10.1029/90JA02464

Spreiter, J. R., Summers, A. L., & Alksne, A. Y. (1966). Hydromagnetic flow around the magnetosphere. *Planetary and Space Science*, *14*(3), 223-253. Retrieved from https://www.sciencedirect.com/science/article/pii/0032063366901243 doi: https://doi.org/10.1016/0032-0633(66)90124-3

Sun, T. R., Wang, C., Sembay, S. F., Lopez, R. E., Escoubet, C. P., Branduardi-Raymont, G., ... Guo, Y. H. (2019). Soft x-ray imaging of the magnetosheath and cusps under different solar wind conditions: Mhd simulations. *Journal of Geophysical Research: Space Physics*, *124*(4), 2435-2450. Retrieved from https://agupubs.onlinelibrary.wiley.com/doi/abs/10.1029/2018JA026093 doi: https://doi.org/10.1029/2018JA026093

Toledo-Redondo, S., Lavraud, B., Fuselier, S. A., André, M., Khotyaintsev, Y. V., Nakamura, R., ... Burch, J. L. (2019). Electrostatic spacecraft potential structure and wake formation effects for characterization of cold ion beams in the earth's magnetosphere. *Journal of Geophysical Research: Space Physics*, *124*(12), 10048-10062. Retrieved from https://agupubs.onlinelibrary.wiley.com/doi/abs/10.1029/2019JA027145 doi: https://doi.org/10.1029/2019JA027145

Tóth, G., Sokolov, I. V., Gombosi, T. I., Chesney, D. R., Clauer, C. R., de Zeeuw, D. L., ... Kóta, J. (2005, December). Space Weather Modeling Framework: A new tool for the space science community. *Journal of Geophysical Research*

(Space Physics), *110*, A12226. doi: 10.1029/2005JA011126

Tóth, G., van der Holst, B., Sokolov, I. V., De Zeeuw, D. L., Gombosi, T. I., Fang, F., ... Opher, M. (2012, February). Adaptive numerical algorithms in space weather modeling. *Journal of Computational Physics*, *231*, 870-903. doi: 10.1016/j.jcp.2011.02.006

Tsyganenko, N. A., & Sibeck, D. G. (1994). Concerning flux erosion from the dayside magnetosphere. *Journal of Geophysical Research: Space Physics*, *99*(A7), 13425-13436. doi: 10.1029/94JA00719

Vasyliunas, V. M., Kan, J. R., Siscoe, G. L., & Akasofu, S.-I. (1982). Scaling relations governing magnetospheric energy transfer. *Planetary and Space Science*, *30*(4), 359–365.

Walsh, B. M., Collier, M. R., Kuntz, K. D., Porter, F. S., Sibeck, D. G., Snowden, S. L., ... Thomas, N. E. (2016). Wide field-of-view soft x-ray imaging for solar wind-magnetosphere interactions. *Journal of Geophysical Research: Space Physics*, *121*(4), 3353-3361. Retrieved from `https://agupubs.onlinelibrary.wiley.com/doi/abs/10.1002/2016JA022348` doi: https://doi.org/10.1002/2016JA022348

Wang, Y., Sibeck, D. G., Merka, J., Boardsen, S. A., Karimabadi, H., Sipes, T. B., ... Lin, R. (2013). A new three-dimensional magnetopause model with a support vector regression machine and a large database of multiple spacecraft observations. *Journal of Geophysical Research: Space Physics*, *118*(5), 2173-2184. Retrieved from `https://agupubs.onlinelibrary.wiley.com/doi/abs/10.1002/jgra.50226` doi: https://doi.org/10.1002/jgra.50226

Wegmann, R., Schmidt, H., Lisse, C., Dennerl, K., & Englhauser, J. (1998). X-rays from comets generated by energetic solar wind particles. *Planetary and Space Science*, *46*(5), 603-612. Retrieved from `https://www.sciencedirect.com/science/article/pii/S0032063397001967` doi: https://doi.org/10.1016/S0032-0633(97)00196-7

Xi, S., Lotko, W., Zhang, B., Brambles, O. J., Lyon, J. G., Merkin, V. G., & Wiltberger, M. (2015). Poynting flux-conserving low-altitude boundary conditions for global magnetospheric models. *Journal of Geophysical Research: Space Physics*, *120*(1), 384-400. Retrieved from `https://agupubs.onlinelibrary.wiley.com/doi/abs/10.1002/2014JA020470` doi: 10.1002/2014JA020470